Microfluid Nanofluid (2006) 2: 455–469
DOI 10.1007/s10404-006-0092-9

RESEARCH PAPER

Jerry M. Chen · Tzyy-Leng Horng · Wei Yee Tan

# Analysis and measurements of mixing in pressure-driven microchannel flow

Received: 1 March 2006 / Accepted: 24 March 2006 / Published online: 25 April 2006


**Abstract** The mixing phenomena for two fluid streams in pressure-driven rectangular microchannels are analyzed and directly compared with the measurements of mixing intensity for a wide range of aspect ratio (width/depth = 1–20). In the analysis, the three-dimensional transport equation for species mixing was solved using the spectral method in a dimensionless fashion covering a large regime of the normalized downstream distance. The analysis reveals the details of non-uniform mixing process, which originates from the top and bottom walls of the channel and stretches out toward the center of the channel, and its transition to uniformity. Employing different length scales for the non-uniform and uniform mixing regimes, the growth of mixing intensity can be expressed in a simple relationship for various aspect ratios in the large range. The mixing experiments were carried out on silicon- and poly(methyl methacrylate) (PMMA)-based T-type micromixers utilizing fluids of pH indicator (in silicon channel) and fluorescent dye (in PMMA channel) to evaluate the mixing intensity based on flow visualization images. Using conventional microscopes, the experiments demonstrate the mixing intensity as a power law of the stream velocity for all the microfluidic channels tested. The variations of measured mixing intensity with the normalized downstream distance are found in favorable agreement with the numerical simulations. The comparison between the experiments and simulations tells the capabilities and limitations on the use of conventional microscopes to measure the mixing performance.

J. M. Chen (✉) · W. Y. Tan
Department of Mechanical Engineering,
National Chung Hsing University, Taichung 402, Taiwan
E-mail: jerryc@dragon.nchu.edu.tw
Tel.: +886-4-22840433
Fax: +886-4-22877170

T.-L. Horng
Department of Applied Mathematics, Feng Chia University,
Taichung 405, Taiwan

**Keywords** Microfluidics · Non-uniform diffusion · Spectral method · Mixing measurement

## 1 Introduction

In the past decade, microfluidic components, devices, and systems have been widely used in biological and chemical analyses. Among a broad range of the applications of these analyses, mixing is essential in the processes of cell activation, enzyme reaction, protein folding, sequencing or synthesis of nucleic acids, and many microfabricated chemical systems involving complex chemical synthesis. The mechanism of mixing two fluid streams in a microscale channel having dimensions of several hundred microns and below is quite different from a macroscale channel. The flow in microchannels is typically laminar because of the small Reynolds number (under 100). As turbulence is absent, mixing at the microscale occurs primarily via molecular diffusion at the interface between the two fluids. It often takes much longer time for complete mixing in micro systems than in the macro systems where turbulence and secondary flow are present. In order to enhance mixing performance in microchannel flow, there are two general types of designs (Stone et al. 2004): (1) passive methods to induce transverse flows via the interaction of the main stream with the specifically designed channel geometry (Branebjerg et al. 1996; Liu et al. 2000; Stroock et al. 2002); (2) active methods to produce transverse flows by oscillatory forcing within the channel (Lee et al. 2001; Deval et al. 2002; Lu et al. 2002; Bottausci et al. 2004; Okkels and Tabeling 2004). Nguyen and Wu (2005) provided a very thorough review on the recent development of various types and designs of passive and active micromixers.

For quantification of the mixing performance in a microchannel, the techniques incorporated with microscopic images of flow visualization of the mixing phenomenon are most frequently employed. Such quantification is based on the idea that physical or

chemical properties of the flow system can be correlated with changes in color or fluorescence intensity of the streams. For example, Branebjerg et al. (1996) chose the reaction of a pH indicating phenol-red and acid to visualize the mixing process; Liu et al. (2000) used sodium hydroxide and phenolphthalein dissolved in alcohol as the working fluids; and Wu et al. (2004) employed a fluorescence microscope for fluorescence mixing evaluation.

However, fundamentals of the designs and insight physics for micromixing are not fully understood. A better understanding of the micromixing mechanism is highly desired to interpret the experimental results and to provide guidance for design of microfluidic devices. One of the important issues which needs to be further addressed is the mixing phenomenon that occurs in a pressure-driven flow. Pressure-driven flow is commonly used in microfluidic applications. The velocity profile of such flow is typically parabolic-like across the fluid–fluid interface in a rectangular micromixer. The parabolic velocity profile could cause a substantial difference in residence time of diffusive transport between the diffusion near the top and bottom walls and in the center of the channel. The variation of diffusion with the position may influence the measurements of mixing intensity and molecular properties as well. Ismagilov et al. (2000) using confocal fluorescent microscopy found that the diffusion broadening region at the top and bottom walls of a rectangular microchannel is significantly wider than that in the center of the channel and scales as the one-third power law of the ratio of the downstream distance to the average flow velocity, instead of the more familiar one-half power measured in the middle of the channel. This non-uniform diffusion is identified as the butterfly effect and the diffusive scaling law has been reported varying between 0.35 and 0.5 across the channel depth by Kamholz and Yager (2001) in a two-dimensional finite difference simulation for the channel with an aspect (width to depth) ratio of 2.36. In fact, the diffusive characteristics depend on the Peclet number, which compares the time scale for diffusive transport to that for convective transport, as well as on the ratio of downstream distance to the channel dimension (Ismagilov et al. 2000). The characteristics are also anticipated to vary with the aspect ratio through the change in velocity profile. In previous studies of basic T- and Y-type mixers, a wide range of aspect ratio (0.5–50) was employed by different authors (Nguyen and Wu 2005). Among these studies, detailed effects of aspect ratio on mixing performance were investigated by Gobby et al. (2001). Their computational study of T-type mixers for gaseous flow reported significant effects of aspect ratio on mixing efficiency only in the large range (for constant channel width with aspect ratio greater than 2). They also found that throttling (i.e. a sudden change to lower aspect ratio) could considerably enhance the mixing. Nevertheless, the effects on mixing performance due to the composite of aspect ratio associated with Peclet number and downstream distance is yet to be addressed.

This study presents a more thorough analysis of the mixing phenomena together with measurements of the mixing intensity for the fluids involving the convection–diffusion process in pressure-driven microchannels with rectangular cross section. The three-dimensional (3D) mixing model analyzed here assumes large Peclet number for which convection dominates the diffusion in the axial direction. The model is solved numerically in a dimensionless fashion that is managed based on the analytical solution to the case of constant convection velocity. The dimensionless variable of normalized downstream distance employed here combines the dimensionless axial distance with the Peclet number, making the aspect ratio of the mixing channel the only parameter in the analysis. The numerical simulations are performed using the spectral scheme with Chebyshev polynomial expansions, which offers much higher-order accuracy than the ordinary finite difference and finite element methods. The Chebyshev polynomials are well suitable for computing the detailed variations near the walls and the interface of fluids (Gottlieb and Orszag 1997). The numerical analysis focuses on the variations of mixing processes with the normalized downstream distance and the change in aspect ratio. In order to investigate for a wider range of channel aspect ratio, the mixing experiments were carried out on silicon- and poly(methyl methacrylate) (PMMA)-based T-type micromixers using fluids of pH indicator (in silicon channel) and fluorescent dye (in PMMA channel) to evaluate the mixing intensity from flow visualization images. The visualization images were acquired using conventional microscopes that, rather than the more expensive confocal microscopy, are commonly used by most investigators to measure the mixing performance. Both the analysis and measurements were made for channels with aspect ratio (width/depth) ranging from 1–20 and covered a large mixing distance down the channel containing the transition from non-uniform to uniform diffusion across the channel depth.

## 2 Mathematical model and numerical method

### 2.1 Formulation

Figure 1 illustrates the model and coordinates used for the present analysis of the mixing phenomenon between fluids A and B in a T-type micromixer. The T-type micromixer has two inlet channels and a single mixing channel. The origin of the coordinates is located at the center of the cross-section of the mixing channel where the fluids start to meet. When these two fluids come to the entrance of the mixing channel with a rectangular cross section $b \times h$, each of the fluids occupies half of the cross-section.

This analysis focuses on the concentration distribution of the two fluid streams in the mixing channel ($z \geq 0$). For the case that fluids A and B have the same viscosity, the velocity profile is symmetric about the

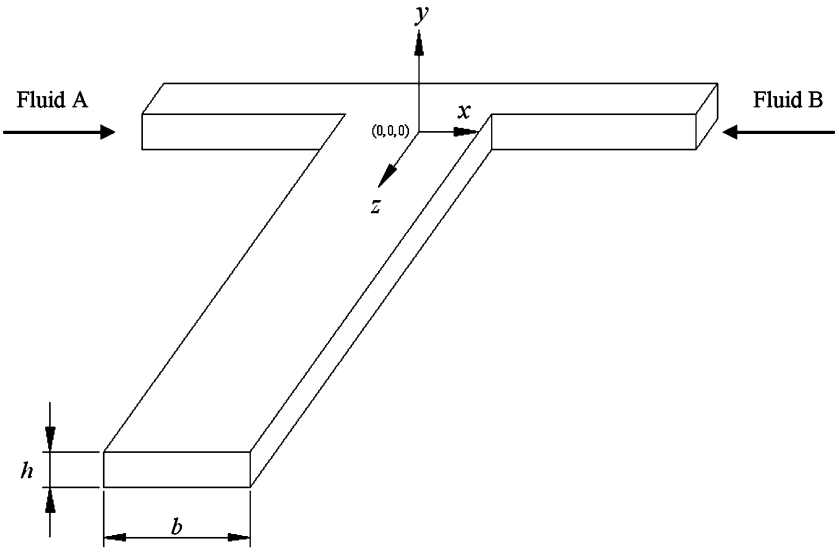


**Fig. 1** Schematic of microchannel and coordinates for numerical simulation

channel midline ($x = 0$). In this situation, we may merely consider the species concentration of fluid A that is on the left half with a constant original concentration $c_0$ mixing with fluid B via convective and diffusive transport on the right half ($0 \le x \le b/2$). The species transport equation for an incompressible fluid is governed by (Bird et al. 1960)

$$\frac{\partial c}{\partial t} + u_x \frac{\partial c}{\partial x} + u_y \frac{\partial c}{\partial y} + u_z \frac{\partial c}{\partial z} = D\left[\frac{\partial^2 c}{\partial x^2} + \frac{\partial^2 c}{\partial y^2} + \frac{\partial^2 c}{\partial z^2}\right] + R \tag{1}$$

where $c$ is the species concentration of fluid A, $u_x$, $u_y$, and $u_z$ are the velocity components in the $x$, $y$, and $z$ directions, respectively, $D$ is the diffusion coefficient, and $R$ is the rate of change of concentration of fluid A produced by chemical reaction. For a steady, non-reactive system, with the assumptions of fully developed flow and large Peclet number (i.e. convection dominates over diffusion in the $z$-direction), Eq. 1 reduces to

$$u_z \frac{\partial c}{\partial z} = D\left[\frac{\partial^2 c}{\partial x^2} + \frac{\partial^2 c}{\partial y^2}\right], \quad \text{for } 0 < x < \frac{b}{2}, \quad -\frac{h}{2} < y < \frac{h}{2}. \tag{2}$$

The above equation is subject to an initial condition of $c = 0$ at the channel entrance ($z = 0$) and zero-flux boundary conditions at the top, bottom, and sidewalls ($y = \pm h/2$, $x = b/2$):

$$\frac{\partial c}{\partial x}\left(\frac{b}{2}, y, z\right) = 0, \qquad \frac{\partial c}{\partial y}\left(x, \pm\frac{h}{2}, z\right) = 0 \tag{3}$$

Moreover, by symmetry, the Dirichlet boundary condition $c = c_0/2$ can therefore be applied to the interface at the channel midline.

Before solving the steady species transport equation in the three-dimensional (3D) form, it is worth looking at the solution to the equation with a much simpler convection velocity of constant $u_z = u_0$ throughout the channel as in the slug flow. The concentration distribution is now independent of $y$ and the equation for the 2D concentration field $c(x, z)$ can be solved analytically to obtain the mixing intensity $I_{\text{mix}}$ by averaging the concentration over the channel width:

$$I_{\text{mix}} = \frac{\bar{c}(z)}{(c_0/2)} = 1 - \frac{8}{\pi^2}\sum_{n=1}^{\infty}\frac{1}{(2n-1)^2}\exp\left[\frac{-(2n-1)^2 Dz}{b^2 u_0}\right] \tag{4}$$

where the average concentration $\bar{c}(z)$ is normalized with the interface concentration $c_0/2$ to represent as the mixing intensity. Details about the analytical solution for the 2D concentration field can be found in Wu et al. (2004) and Nguyen and Wu (2005). The mixing intensity given in Eq. 4 shows a well-known constant growth rate of 0.5 (one-half power) of the downstream distance $z$ until $I_{\text{mix}}$ becomes large (around 54%) as the dimensionless group $Dz/(b^2u_0)$ arrives a value of $10^{-0.25}$. Subsequently, the growth rate decreases with a further increase in $z$ to approach the state of complete mixing ($I_{\text{mix}} = 99\%$ at $Dz/(b^2u_0) = 10^{0.65}$).

When one attempts to non-dimensionalize Eq. 2 for 3D calculations, the solution of Eq. 4 also hints that it is natural and convenient to use a normalized downstream distance of the form

$$Z^* = \frac{Dz}{b^2 u_0}, \tag{5}$$

hereafter $u_0$ denotes the average velocity in 3D cases. The Peclet number ($Pe = bu_0/D$) is now contained in $Z^*$ together to form a single dimensionless variable in the expression of the growth of mixing. By letting

$$C = \frac{c}{(c_0/2)}, \quad X = \frac{x}{b}, \quad Y = \frac{y}{h}, \tag{6}$$

the dimensionless formulation for Eq. 2 yields

$$U_z \frac{\partial C}{\partial Z^*} = \frac{\partial^2 C}{\partial X^2} + \gamma^2 \frac{\partial^2 C}{\partial Y^2}, \quad \text{for } 0 < X < 0.5, \quad -0.5 < Y < 0.5, \tag{7a}$$

with the boundary and initial conditions,

$$C(0, Y, Z^*) = 1, \frac{\partial C}{\partial Y}(X, \pm 0.5, Z^*) = \frac{\partial C}{\partial X}(0.5, Y, Z^*) = 0, \; C(X, Y, 0) = 0, \tag{7b}$$

where $U_z = u_z/u_0$ is the normalized axial flow velocity, $\gamma = b/h$ is the aspect ratio. Notably, the aspect ratio is the only parameter that appears in Eqs. 7a, 7b.

For fully developed flow of uniform viscosity in a rectangular cross-sectional channel, the velocity profile $U_z$ ($X$, $Y$) can be obtained analytically (White 1974):

$$U_z = \frac{\pi}{4}\left[\sum_{k=1,3,5,\ldots}^{\infty} \frac{1}{k^4}\left[\frac{\gamma}{2k\pi}\tanh\left(\frac{k\pi}{2\gamma}\right)\right]\right]^{-1} \sum_{k=1,3,5,\ldots}^{\infty} \frac{(-1)^{\frac{k-1}{2}}}{k^3}\left[1 - \frac{\cosh(k\pi Y/\gamma)}{\cosh(k\pi/2\gamma)}\right]\cos(k\pi\ X). \tag{8}$$

The velocity profiles given by the above equation always show a parabolic distribution across the $Y$ dimension on the channel midline ($X = 0$). For the case of larger aspect ratio, a large portion of the channel width (e.g. $-0.33 \le X \le 0.33$ for $\gamma = 10$) is described by the parabolic profile

$$U_z = \frac{3}{2}(1 - 4Y^2), \tag{9}$$

as in the fully developed 2D flow and then followed by a sharp drop to zero at the sidewalls ($X = \pm 0.5$). For the case of smaller aspect ratio ($\gamma \sim 1$), this parabolic profile falls gradually with the distance from the channel midline to approach the no-slip boundary condition at the sidewalls.

## 2.2 Numerical method

We employ the method of lines (MOL) by the Chebyshev pseudospectral technique for spatial discretization in $X$–$Y$ domain together with a stiff ODE solver for $Z^*$-direction integration to solve Eqs. 7a, 7b with the associated boundary conditions and initial condition. The Chebyshev polynomials are well suitable for the present computational study that requires high resolutions neighboring the walls and the interface of the mixing fluids (Gottlieb and Orszag 1997). In order to accommodate the Chebyshev polynomials, the physical $X$–$Y$ domain $[0,0.5] \times [-0.5,0.5]$ is mapped to the computational $\xi$ –$\eta$ domain $[-1,1] \times [-1,1]$ through the following linear mapping

$$\xi = 4(X - 0.25), \quad \eta = 2Y. \tag{10}$$

Therefore, Eq. 7a becomes

$$U_z \frac{\partial C}{\partial Z^*} = 16\frac{\partial^2 C}{\partial \xi^2} + 4\gamma^2 \frac{\partial^2 C}{\partial \eta^2}, \tag{11a}$$

with the boundary and initial conditions becoming

$$C(-1, \eta, Z^*) = 1, \quad \frac{\partial C}{\partial \eta}(\xi, \pm 1, Z^*) = \frac{\partial C}{\partial \xi}(1, \eta, Z^*) = 0, \quad C(\xi, \eta, 0) = 0, \tag{11b}$$

The concentration $C(\xi, \eta, Z^*)$ is then approximated by a truncated double series of Chebyshev polynomials in $\xi$ and $\eta$, and Eqs. 11a, 11b are discretized in $\xi$–$\eta$ space as

$$U_z(\xi_i, \eta_j)\frac{\partial C}{\partial Z^*}(\xi_i, \eta_j, Z^*) = 16\frac{\partial^2 C}{\partial \xi^2}(\xi_i, \eta_j, Z^*) + 4\gamma^2 \frac{\partial^2 C}{\partial \eta^2}(\xi_i, \eta_j, Z^*), \quad i = 1, 2, \ldots, M-1, \; j = 1, 2, \ldots, N-1, \tag{12}$$

Details about the discretization with the Chebyshev polynomials are given in Appendix 1.

After the discretization of Eq. 12 in $\xi$ and $\eta$, the governing PDE (Eq. 11a) and the associated boundary conditions (Eq. 11b) become a coupled system of ODEs (with respect to $Z^*$) and algebraic equations (associated with the boundary conditions). The whole coupled differential-algebraic equations (DAEs) are expressed in concise mathematical form

$$\mathbf{M}\frac{\partial C(\xi_i, \eta_j, Z^*)}{\partial Z^*} = f(\xi_i, \eta_j, Z^*), \tag{13}$$

where $\mathbf{M}$ is the diagonal mass matrix, of which the diagonal element is 1 corresponding to the ODE part ($Z^*$ dependence) and 0 to the algebraic equation part (no $Z^*$ dependence due to boundary conditions). Equation 13 is an index-1 DAEs that can be solved by any suitable DAE solver. Here, we used MATLAB function ode15s, which is a variable-order solver based on the numerical differentiation method NDFs.

One last thing to deal with is the incompatibility between the boundary condition at $\xi = -1$ and the initial condition. This discontinuity will cause strong spurious oscillation in numerical result due to the nature of Chebyshev pseudospectral discretization called Gibb's phenomenon. Therefore, we smoothed this discontinuous initial condition by fitting a boundary layer in Gaussian function shape

$$C(\xi, \eta, 0) = \exp\left(-\left(\frac{\xi + 1}{\theta}\right)^2\right), \tag{14}$$

where $\theta$ denotes the thickness of boundary layer. Hence, the only requirement of resolution in $\xi$ - $\eta$ space is to resolve this boundary layer well.

Since the Chebyshev pseudospectral method is a much higher-order method in accuracy compared with the ordinary finite difference and finite element methods used by most of the commercially available packages, a saving of resolution in $\xi$–$\eta$ space is expected. In the present study, efficient and satisfactory results were obtained with the spatial resolution $M = 24$ and $N = 120$ running on a PC with a 1.4 GHz Intel processor.

## 3 Numerical results and discussion

### 3.1 Mixing intensity and concentration distribution

Figure 2 shows the log–log plots of the mixing intensity versus $Z^*$ at difference vertical locations for aspect ratios $\gamma = 1$ and 10. The mixing intensity $I_{\text{mix}}$ is computed from the concentration following the integration

$$I_{\text{mix}}(Y, Z^*) = \int_{-0.5}^{0} C'(X, Y, Z^*)\mathrm{d}X + \int_{0}^{0.5} C(X, Y, Z^*)\mathrm{d}X, \tag{15}$$

where $C'$ is the species concentration of fluid B and can be obtained by symmetry from $C$. The variations of mixing intensity in both cases show a common trend that $I_{\text{mix}}$ is small (less than 1.3%) as $Z^*$ is on the order of $10^{-6}$ and then grows with a power value mostly between 0.33 and 0.54 until it levels off to approach complete (~100%) mixing around $Z^* = 0.1$. It is found that the power value depends not only on $Y$ but also on $Z^*$ and $\gamma$. For certain ranges of $Z^*$, the power values may be approximated using the linear fits. For $\gamma = 1$, the approximated power value in the range of $Z^*$ from $10^{-5}$ to $5.0 \times 10^{-2}$ increases from 0.35 at $Y = 0.5$ (the surface) to 0.5 at $Y = 0.4$, and then rises slightly to 0.54 at $Y = 0.25$ and $Y = 0$ (the center). For $\gamma = 10$, the curves of $I_{\text{mix}}$ for various values of $Y$ merge to form a single curve beginning at $Z^* = 2.0 \times 10^{-3}$ well before the complete mixing. The merger of all curves indicates uniform mixing intensity across the $Y$ dimension. The curve in the range of uniform mixing follows the one-half power, while in the range of non-uniform mixing ($Z^* < 2.0 \times 10^{-3}$) the curves are found to become steeper as $Y$ decreases from the surface to center. The power values in the range of non-uniform mixing are approximately 0.33, 0.42, 0.50, and 0.54 at $Y = 0.5$, 0.4, 0.25, and 0, respectively. Note that for both cases, the power value could slightly exceed 0.5 when measured near the center. Furthermore, the surface mixing intensity is apparently higher than those of other $Y$ positions at the same $Z^*$ before the uniform mixing is reached. The difference between $I_{\text{mix}}$ at the surface and other $Y$ positions is particularly significant for the smaller aspect ratio and small $Z^*$. This significant difference is due largely to the velocity profile. For a smaller aspect ratio, the sidewall effect on the convective velocity can extend to nearing the channel midline, causing a larger

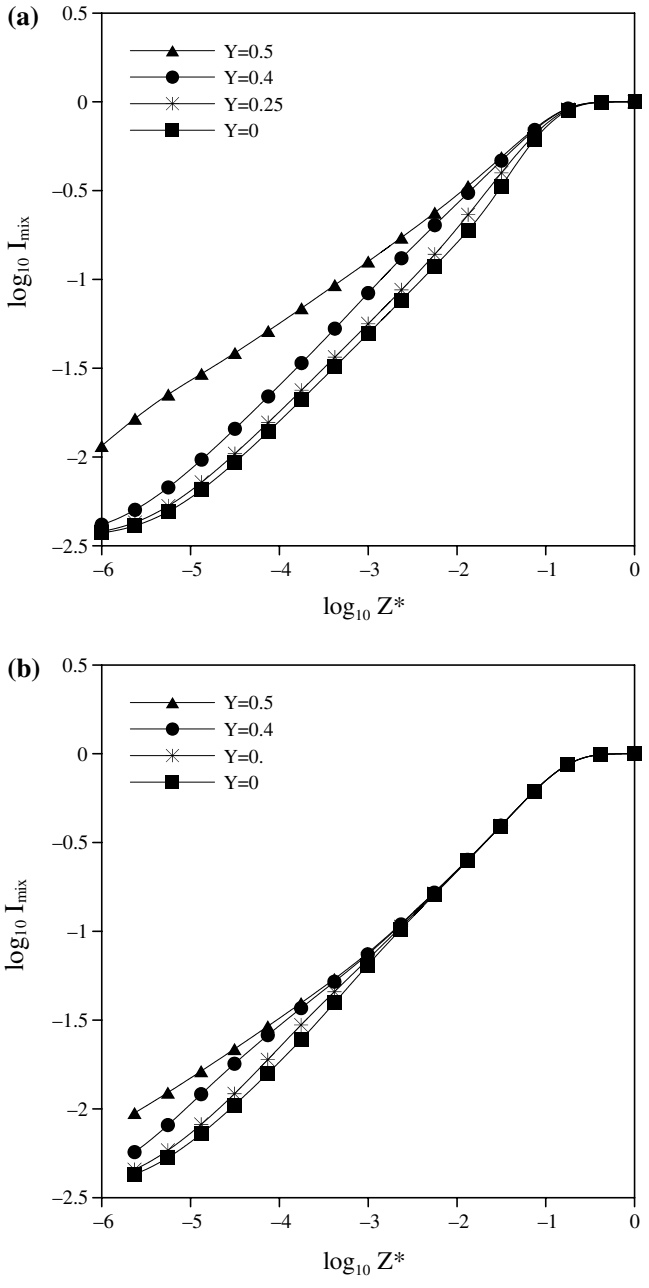


**Fig. 2** Variation of mixing intensity with normalized downstream distance $Z^*$ for **a** $\gamma = 1$ and **b** $\gamma = 10$

maximum normalized velocity (2.096 for $\gamma = 1$ and 1.601 for $\gamma = 10$ from Eq. 8). As a result, the difference in residence time for diffusion between the fluids near the surface and the center is enlarged.

As indicated in Fig. 2, the concentration distribution may not be uniform across the channel depth. It is interesting to examine the concentration distribution over a cross section at certain particular downstream locations. Figures 3 and 4 compare the cross-sectional concentration distributions computed at various values of $Z^*$ for $\gamma = 1$ and 10, respectively. The concentrations shown in the figures are $C$ on the right half

($0 \leq X \leq 0.5$) and $C$' on the left half ($-0.5 \leq X \leq 0$). For $\gamma = 1$, the "butterfly effect" that displays larger transverse ($X$-direction) mixing region near the top and bottom surfaces than at the center is visible at all the normalized downstream locations presented. As can be seen for smaller $Z^*$, the non-uniformity in mixing region begins from the surfaces. As $Z^*$ increases to $10^{-2.5}$ and $10^{-1.5}$, the mixing region becomes wider and the non-uniformity extends toward the center of the channel. For the larger aspect ratio $\gamma = 10$, the butterfly effect is visible only at smaller $Z^*$ ($= 10^{-4.5}$ and $10^{-3.5}$). The mixing region becomes uniform across the depth as $Z^*$ increases to $10^{-2.5}$ and $10^{-1.5}$. Notice that Fig. 4c, d are close-ups of Fig. 4a, b with the $X$ scale narrowed between $-0.05$ and 0.05 and the $Y$-scale held unchanged, making the pictures a dimensional width to height ratio of 1:1 which clearly show the non-uniform mixing region across the depth.

In the preceding discussion, we used the mixing intensity to characterize the quantity of mixing ability between two fluid streams. Alternatively, the mixing ability is characterized in terms of width of interdiffusion zone, or of different names, such as diffusive displacement, extent of diffusion, diffusion broadening, and width of the region mixed by diffusion, referred by different authors (Ismagilov et al. 2000; Kamholz and Yager 2001). The width of diffusion region $\delta$ is a measure of the distance of diffusive mixing across the fluid–fluid interface with the concentration intensity above a cutoff value. Figure 5 shows the ratio of the width of interdiffusion region to the channel width as a function of $Z^*$ for different cutoff concentration values (20–80%)

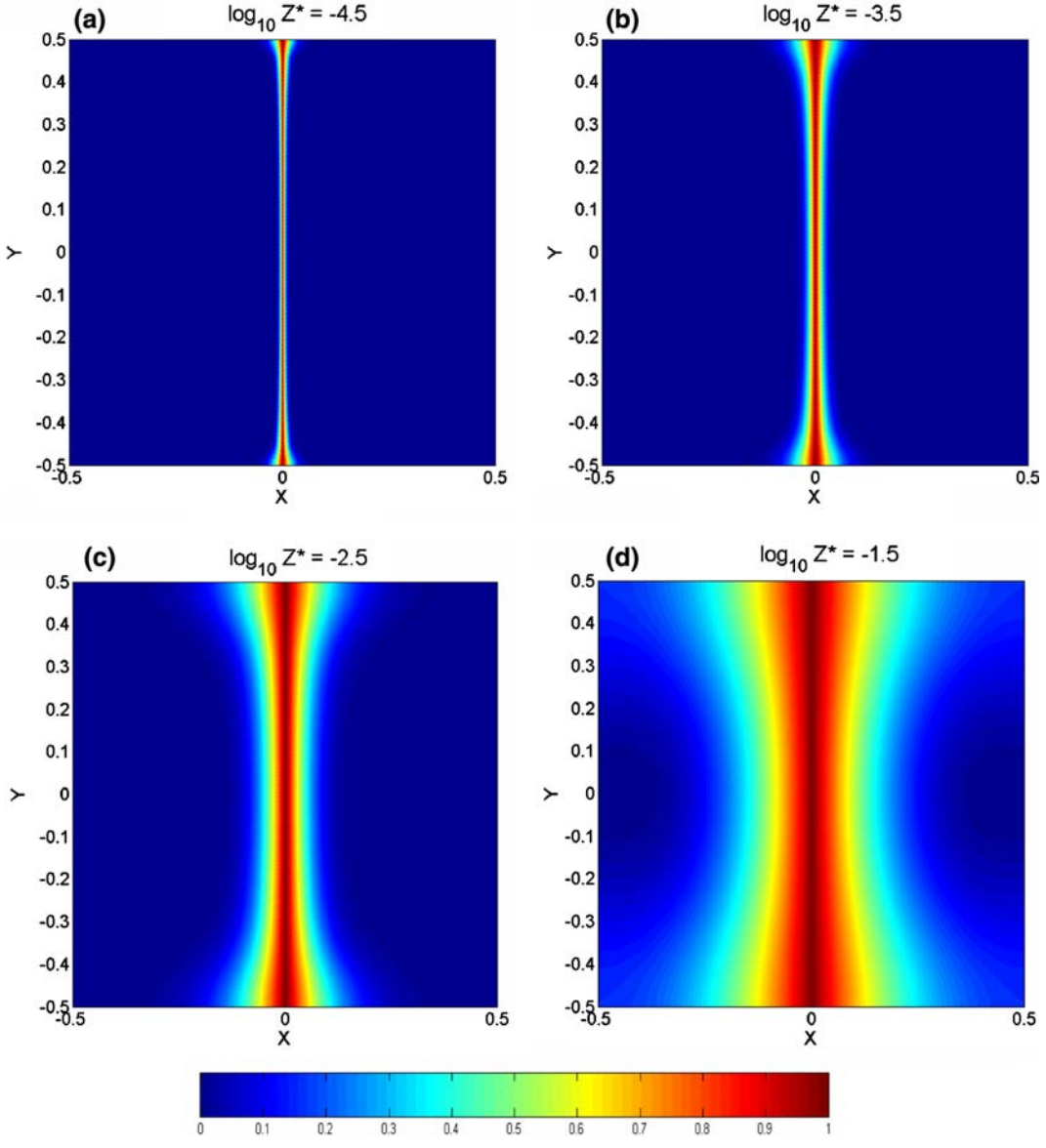


**Fig. 3** Cross-sectional distribution of concentration for $\gamma = 1$ at different normalized downstream distances

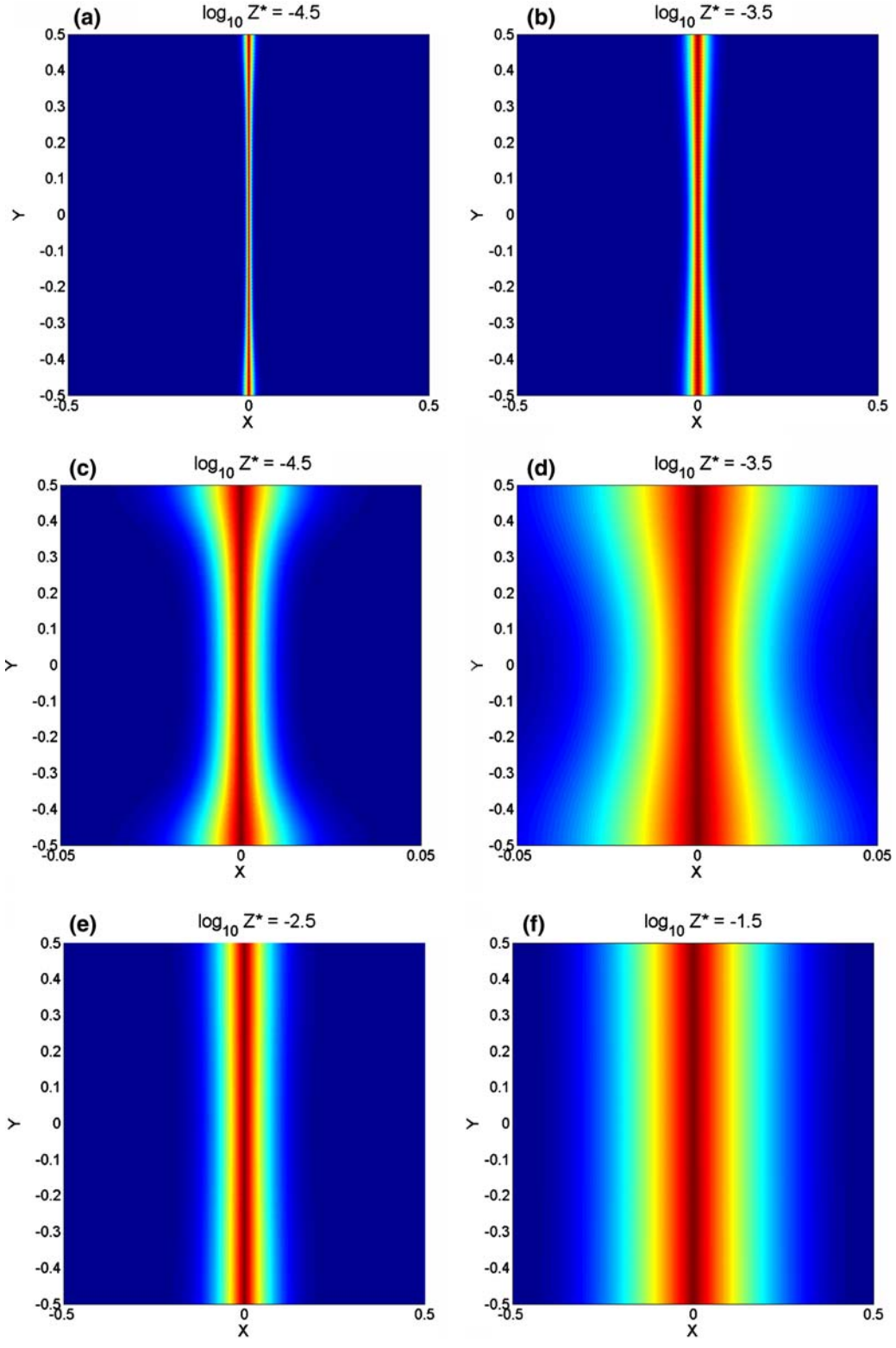


**Fig. 4** Cross-sectional distribution of concentration for $\gamma = 10$ at different normalized downstream distances, where (**c**) and (**d**) are close-up in $Y$-direction for (**a**) and (**b**), respectively

for $\gamma = 1$ and 10. The width of interdiffusion region displayed in the figure was evaluated at the surface ($Y = 0.5$). Also included in the figure is the curve of mixing intensity $I_{\text{mix}}$. It can be seen that the slopes, representing the mixing growth power values, are essentially the same for all the curves presented. This

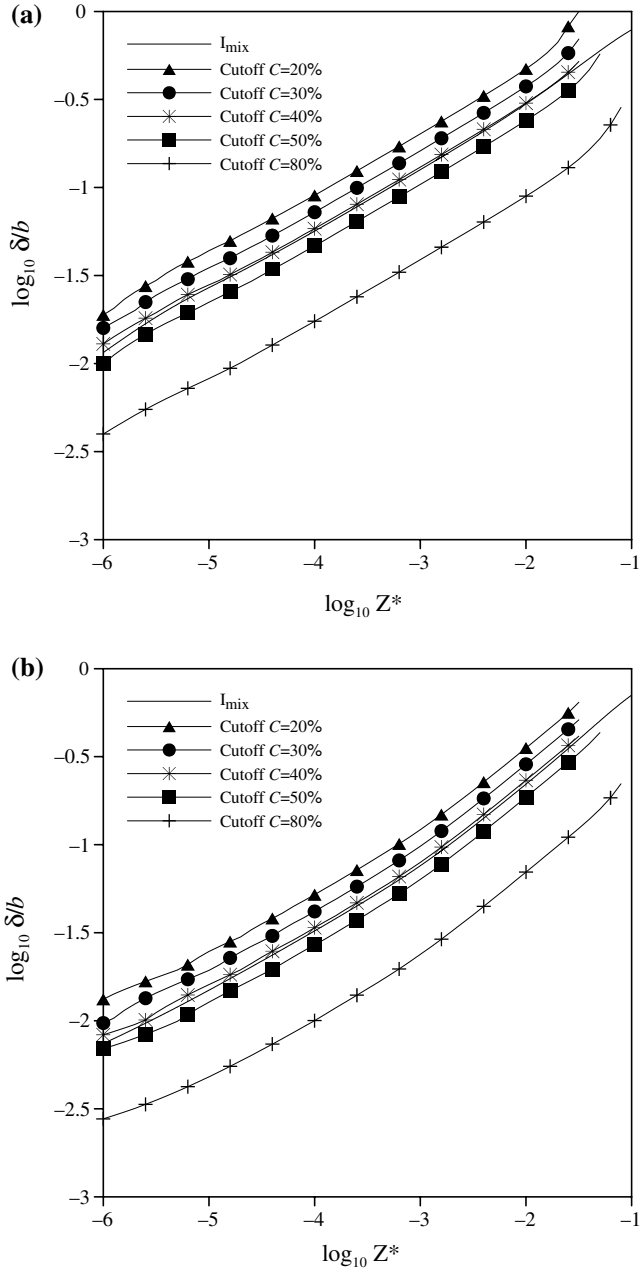


**Fig. 5** Variation of width of diffusion zone $\delta$ at the surface ($Y = 0.5$) with normalized downstream distance $Z^*$ for the intensity above different cutoff values (20–80%): **a** $\gamma = 1$; **b** $\gamma = 10$

indicates the consistence of using $I_{mix}$ and $\delta$ to describe the nature of mixing process. It is worth noting that the curve of $I_{mix}$ is found to coincide with that of $\delta/b$ with a cutoff concentration of 42%.

## 3.2 Aspect ratio effect and scaling characteristics

Figure 6 illustrates the ratio of mixing intensity at the surface to that at the center for different aspect ratios. This figure indicates that both the aspect ratio and $Z^*$ influence the mixing intensity ratio. The mixing ratio of unity means uniform concentration across the $Y$ dimension. On the other hand, large mixing ratio signifies a pronounced difference in the mixing process undergoing between the surface and the center. For small aspect ratios ($\gamma = 0.5$–2), the mixing ratio increases from a value of about 3 at $Z^* = 10^{-6}$ to reach a maximum of 3.8–5.2 nearing $Z^* = 10^{-5}$, and then falls off to a level of 1.0. For large aspect ratios ($\gamma = 5$–20), the variations of mixing ratio all display a similar variation but with lower maximum values and earlier falling off for larger aspect ratios. The similarity in mixing variation for large aspect ratios suggests that it is likely to reconstitute the variables that even combine the aspect ratio in mixing intensity analysis, as the parabolic velocity profile $U_z = 1.5(1-4Y^2)$ of Eq. 9 occupies a wide portion of the channel. Computing with the parabolic velocity for concentration of Eq. 7a, Fig. 7 shows the mixing intensity as a function of the downstream distance with a shift in both ordinate and abscissas axes for $\gamma = 5$–80. The new ordinate log $Z^+$ re-normalizes the downstream distance based on the channel depth instead of the channel width as $Z^+ = Dz/(h^2 u_0)$, and the new abscissas adds the logarithmic mixing intensity by a value of log $\gamma$. Appendix 2 gives the details of the scaling analysis for the coordinate shift. The figure now shows that the curves obtained for all aspect ratios ($\gamma = 5$–80) at $Y = 0.5$, 0.4, and 0 coincide and join together around $Z^+ = 10^{-0.25}$ ($\approx 0.5$). This indicates that the mixing progress for channels with different aspect ratios ($\gamma_1$ and $\gamma_2$) follows the relationship

$$\gamma_1 I_{mix,1}(Y, Z^+) = \gamma_2 I_{mix,2}(Y, Z^+) \tag{16}$$

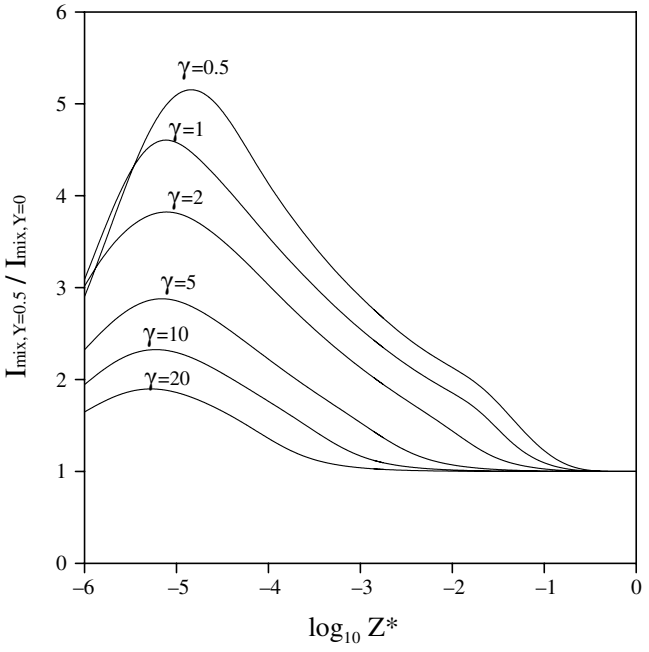


**Fig. 6** Ratio of mixing intensity computed at the surface ($Y = 0.5$) to the center ($Y = 0$)

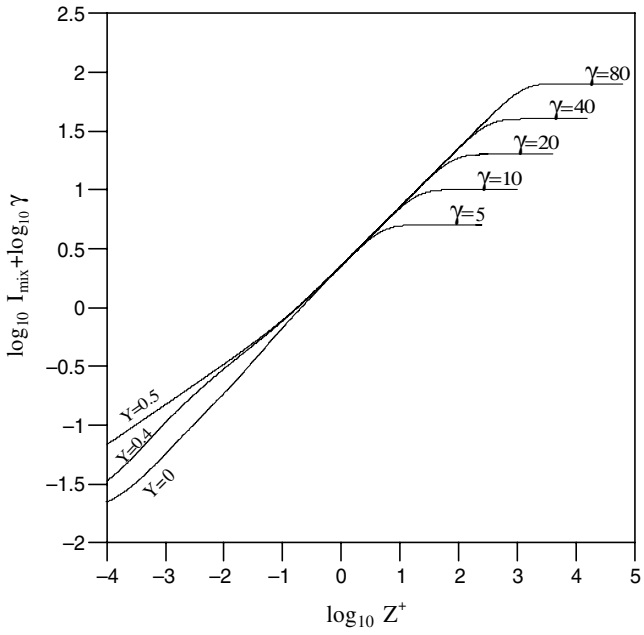


**Fig. 7** Mixing intensity for channels with large aspect ratios as a function of the normalized downstream distance $Z^+ = Dz/(h^2u_0)$ scaled on the channel depth. The vertical coordinate is added by log $\gamma$ to log$I_{\text{mix}}$ to demonstrate that the curves for $\gamma = 5-80$ all coincide with each other before the growth of mixing intensity levels off to approach complete mixing

for large aspect ratios ($\gamma \geq 5$) and mixing intensity in the range of $I_{\text{mix}} \leq 55\%$. The above relationship may be extended to $55\% \leq I_{\text{mix}} \leq 70\%$ for $\gamma \geq 5$ with an error of within 1.5%. Beyond $I_{\text{mix}} = 70\%$, the growth of mixing levels off to reach an asymptotic value of complete mixing so the relationship is no longer valid. Equation 16 may be applied to the cases with smaller aspect ratios ($\gamma < 5$) but with more significant error (approximately 4% for $\gamma = 1$) due mainly to the parabolic velocity profile of Eq. 9 used in the computation of concentration distribution. This simple relationship between aspect ratio and mixing intensity is consistent with the results of Gobby et al. (2001) for the large aspect ratio range ($\gamma \geq 2$) but offers more details in the dependence on $Y$ and $Z^+$. The growth rates for small $Z^+$ ($\leq 10^{-1}$) are approximated 0.34, 0.51, and 0.53 at $Y = 0.5$, 0.4 and 0. Once the mixing is uniform across the $Y$ dimension in the regime of $Z^+ \geq 0.5$, the mixing intensity grows at a power value of 0.5 until it decreases to approach the complete mixing state as described by Eq. 4 for the uniform velocity case. In other words, the growth of mixing is scaled on $Z^*$ rather than on $Z^+$ in the uniform mixing regime.

## 4 Experiments

### 4.1 Experimental setup

The variation of mixing intensity with the distance $Z^*$ down the channel was examined experimentally in T-type mixers as the one depicted in Fig. 1. The experiments were carried out for a wide range of channel aspect ratio. The microfluidic channels with larger aspect ratios ($\gamma$ = 5–20) were fabricated on a silicon substrate, while the square channel ($\gamma$ = 1) was fabricated on a poly(methyl methacrylate) (PMMA) substrate. We first describe the experimental procedures for the silicon-based channels on which most of the concentration measurements were made.

All of the silicon-based channels have a width of 500 μm at the channel surface, a length of 5 mm for each of the inlet channels for fluids A and B, and a length of 15 mm for the mixing channel. The channels of the micromixers were fabricated using the KOH anisotropic etching technique in 4-in silicon wafers. A 1-μm thick oxide was first thermally grown on both sides of the wafers. A positive photoresist (AZ-4620, Clariant, Japan) was then spin coated, heat baked, and exposed to ultraviolet light using a patterned mask. The pattern was then printed on the oxide layer. The silicon wafer was wet-etched with KOH after the oxide layer had been removed using hydrofluoric acid. When the etching process was complete, the wafer was enclosed by anodically bonding a Pyrex#7740 glass (500 μm thick and 100 mm in diameter) to the silicon wafer. The glass covered wafer was then diced into individual microfluidic chips (36 mm × 40 mm) for concentration measurements. For more details on the fabrication processes for silicon-based microchannels, we can refer to Senturia (2001). Microchannels with three different depths $h$ = 26, 55, and 100 μm were utilized for the present experiments. The channel cross sections are of trapezoidal shape due to the nature of KOH etching, and the three cross sections are referred to as aspect ratios $\gamma$ = 20, 10, and 5, respectively.

For the mixing experiments, two separate fluid streams were injected into the fluidics through the inlet channels of the T-type micromixer. One fluid contained phenolphthalein ($C_6H_4COOC(C_6H_4-4-OH)_2$) dissolved in 99% alcohol, with a concentration of 0.031 mol/L. The other fluid contained sodium hydroxide (NaOH) dissolved in 99% alcohol, with a concentration of 0.25 mol/L and a pH of 13. The phenolphthalein changes from colorless to red, as the pH of the solution exceeds 9. A single syringe pump (KDS200, KD Scientific) was employed to drive the two solutions, filled in two syringes, through tubings into the inlet channels. Identical syringes were used to produce equal flow rate for the two inlet fluid streams. The volumetric flow rates produced by the syringe pump can be controlled between 0.001 $\mu$L/h to 147 mL/min with accuracy within ± 1%.

The mixing ability of the phenolphthalein and sodium hydroxide streams were quantified from the concentration distribution of the reacted phenolphthalein that changes color during the mixing process. Figure 8 illustrates the setup for concentration measurements. The images of the mixing fluid streams were acquired using a microscope (10× objective, Mitsutoyo) in

conjunction with an image acquisition and processing system consisting of a CCD camera (VCC-8350A, 640 pixels × 480 pixels, CIS), a frame grabber (Meteor II MC, Matrox), and a PC (Pentium II 500 MHz). The microscope lens has a depth of focus of 3.5 μm and a working distance of 33.5 mm. A halogen lamp (MHF-M1001, Moritex) was used as the light source to produce coaxial light for the optical visualization. The light was relayed through the microscope objective lens into the microfluidic chip. To minimize disturbance introduced by the surroundings, the experiments were carried out on a shock absorber table.

The square microchannel was made of patterned photoresist material (polymer from JSR Corporation) sandwiched between poly(methyl methacrylate) (PMMA) substrates. Using photoresist for microfluidic fabrication has been reported to provide not only better control of channel dimensions but also simpler fabrication processes than molding fabrication (Chen et al. 2003; Horng et al. 2005). The PMMA/photoresist/PMMA sandwich technique is well suitable for fabrication of low aspect ratio ($\gamma \approx 1$) and optical accessible microfluidic channels. One can refer to Horng et al. (2005) for fabrication details about the PMMA-based microchannels. The setup for optical visualization of mixing phenomenon in the square microchannel was the same as that shown in Fig. 8 for the silicon-based channels, except for the mixing fluids and the microscope. For the mixing visualization in the PMMA-based channel, the two fluids used were DI water and sodium phosphate ($NaH_2PO_4$) buffer (0.01 M, pH = 7.4) with 0.76 mM fluorescent dye (F7505, Sigma-Aldrich, Germany). The excitation and emission wavelengths of the fluorescent dye are 475–490 and 510–520 nm, respectively. The flow images were taken under an epi-fluorescence microscope ($\mu$ Image 1600) with a mercury lamp as the light source.

The concentration measurements were taken at $z = 5$ and 15 mm for the silicon-based channels, and at $z = 15$ mm for the PMMA-based channel. The size of imaged area for each view window of the two downstream locations was 640 μm × 480 μm.

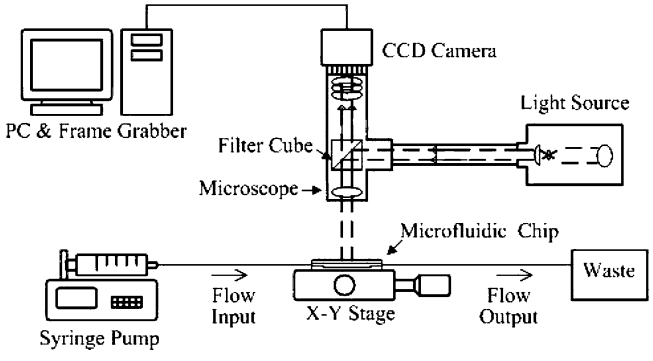


**Fig. 8** Schematic of experimental setup

## 4.2 Quantification of mixing efficiency

The technique of quantifying mixing performance from the concentration measurements is similar to that used by Liu et al. (2000). First, each of the recorded visualization images was transferred into a matrix form that contained the RGB color levels (0–255) for all pixels. Then, the color levels of each pixel in the matrix were rescaled to a value between 0 and 1, which is referred to as the pixel color intensity $l_i$ in pixel $i$. The value of $l_i$ is 1 for brightest color and 0 for the darkest color.

During the convective–diffusive mixing process in the silicon-based microchannel, the phenolphthalein changes to red as it reacts with sodium hydroxide. The quantity of the reacted phenolphthalein in the imaged region at a certain view window is taken to be proportional to the intensity of red integrated over the window image. The intensity of red for a window image is represented by averaging the integral as

$$I = \frac{1}{N_p}\sum_{i=1}^{N_p} l_i, \tag{17}$$

where $I$ is the averaged red intensity for a window image, and $N_p$ is the total number of pixels in the window image. Notably, the red intensity of an image $I$, which does not necessarily prorate the red value of the recorded image, is an indicator of the relative quantity of the reacted phenolphthalein rather than an index of mixing efficiency. In order to obtain the mixing efficiency $\eta_{mix}$, the red intensity is normalized with the maximum and minimum red intensity. The maximum red intensity $I_{max}$ is observed in a fully mixed image, and the minimum intensity $I_{min}$ is observed in an alcohol image. The mixing efficiency is thus given by

$$\eta_{mix} = \frac{I - I_{min}}{I_{max} - I_{min}} \times 100\%. \tag{18}$$

Here, the term "mixing efficiency" instead of "mixing intensity" is used to designate the ability of mixing measured in the present experiments. The measurements of mixing efficiency for the square microchannel follows the same procedures but based on the fluorescence emission instead of red intensity for the window image.

Prior to the measurements of mixing efficiency for the results presented, the validity of Eq. 18 was tested for discrepancies caused by the experimental conditions including dye concentration and the use of different RGB values for the pixel intensity. The method of Eq. 18 to quantify the mixing efficiency from the pixel intensity implies a linear relationship between these two. In the flow rate range tested in the present experiments, the linear relationship held well (within ± 2%) as we varied the aforementioned dye concentration values by a range of ± 30%. It was found that using the red value or taking the average of RGB values for the pixel intensity only causes a difference of less than 1.6% in $\eta_{mix}$ for the cases with phenolphthalein. All of the

mixing efficiencies reported here were computed from the pixel intensity of averaged RGB values. Moreover, the mean local pixel intensity was obtained with a total of 180 image frames for each view window measurement. This number of image frames was a compromise between overall measurement time and accuracy. The estimated uncertainty (due to random errors) of measured intensity values was within ± 1.1%. Limited by the channel resistance and the strength of joints and bonding, the output flow rates for the present experiments were varied between 0.2 and 40 mL/h for the silicon-based microfluidic chips and between 0.2 and 10 mL/h for the PMMA-based chip. The corresponding Reynolds number ranges are 0.5–25, 0.12–24, 0.13–26, and 0.14–28 for $\gamma = 1$, 5, 10, and 20, respectively.

### 4.3 Experimental results and comparison with simulation

Figure 9 shows the variation of mixing efficiency with the average flow velocity in the mixing channel for different aspect ratios. The symbols are the experimental data and the lines represent the linear regression that fits to the data. It can be seen that the mixing efficiency decreases as a power law (i.e. linearly in the log–log plot) of the stream velocity. Except for the case of $\gamma = 5$, the slope values of the regression lines are essentially the same at $-0.34 \pm 0.02$ for all the microchannels presented. The slope values are $-0.40$ and $-0.45$ for $\gamma = 5$ at $z = 5$ and 15 mm, respectively. The larger slope magnitude for $\gamma = 5$ may be due to the fact that mixing is nearing the uniform diffusion regime as will be seen next in the direct comparison of the experimental results with the simulations. Another likely explanation for the larger slopes is the presence of the trapezoidal edges in which the velocity becomes significantly different from the upright geometry as the interdiffusion width approaches the sidewalls (Qu et al. 2000).

Figure 10 compares the numerical simulations with the experimental results, in which the experimental parameters of flow velocity ($u_0$), channel width, and imaged location ($z$) along with diffusion coefficients $D = 4.0 \times 10^{-10}$ m$^2$/s for fluorescent dye and $D = 5.0 \times 10^{-9}$ m$^2$/s for hydroxide ion to phenolphthalein solution (Lide 1994) are combined to form the normalized downstream distance ($Z^*$ or $Z^+$). The numerical simulations, computed as in Fig. 2a for $\gamma = 1$ and Fig. 7 for $\gamma = 5$, 10, and 20, contain the variations of mixing intensity with the normalized downstream distance at the surface ($Y = 0.5$) and center ($Y = 0$) as well as the average mixing intensities. The average mixing intensity is obtained by integration of dimensionless concentration over the entire channel cross section ($X$ and $Y$ directions). For $\gamma = 1$, most of the measured data are in the non-uniform mixing regime, where the simulation calculated at the surface appear to better portray the experimental results than those at the center or the average intensity. For larger aspect ratios $\gamma = 5$, 10, and 20, it might be noted that the channels used in the experiments have trapezoidal cross-sections with bottom width to top width ratios of 0.72, 0.85, and 0.93, respectively. Here, we compare the experimental results of mixing efficiency with the numerical simulations based on rectangular channels rather than those of

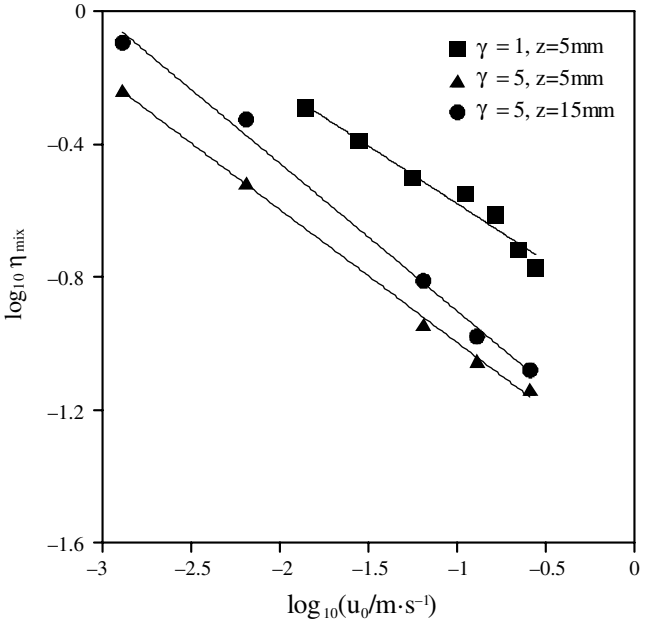


**(a)** γ = 1 and 5

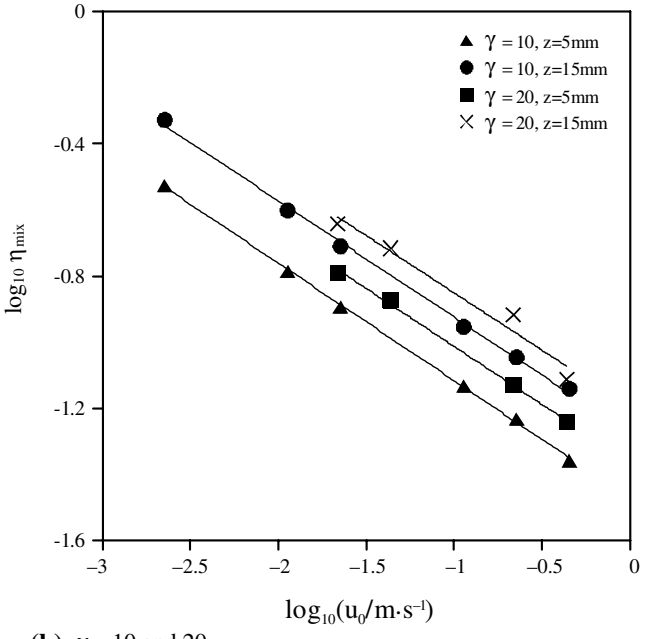


**(b)** γ = 10 and 20

**Fig. 9** Dependence of measured mixing efficiency on average velocity for **a** $\gamma = 1$ and 5, **b** $\gamma = 10$ and 20. Slope values for $\gamma = 1$, 10, and 20 are essentially the same at $-0.34 \pm 0.02$. Slope values for $\gamma = 5$ at $z = 5$ and 15 mm are $-0.40$ and $-0.45$, respectively

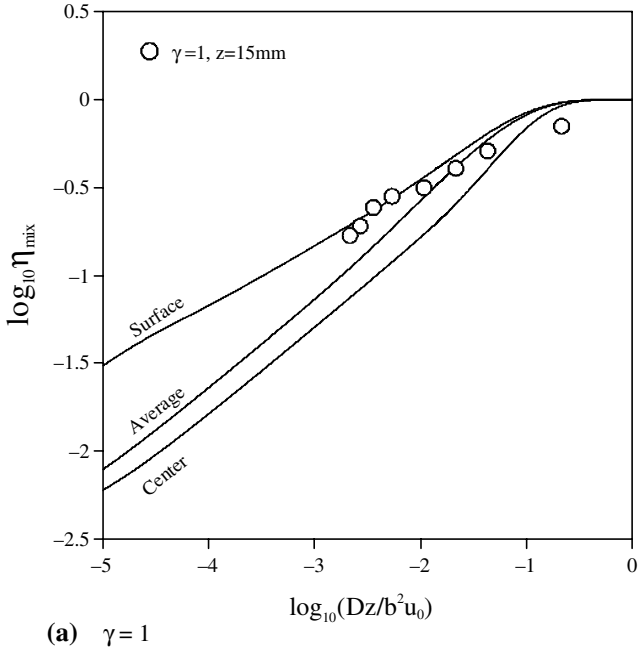


**(a)** $\gamma = 1$

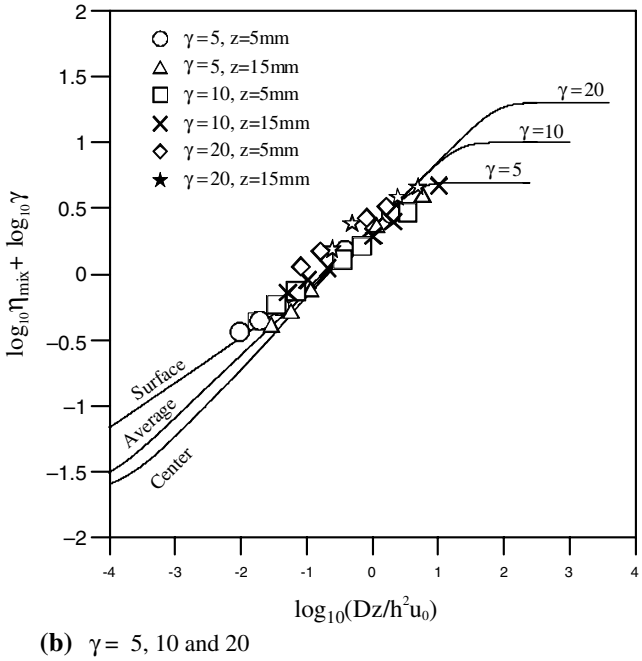


**(b)** $\gamma =$ 5, 10 and 20

**Fig. 10** Comparison of experimental results with numerical simulations: **a** $\gamma = 1$, where the convection velocity of Eq. 8 is used in the simulations. The horizontal coordinate is scaled on the channel width. **b** $\gamma = 5$, 10 and 20, where the convection velocity of Eq. 9 is used in the simulations. The *horizontal coordinate* is scaled on the channel depth and the *vertical coordinate* is shifted to accommodate the mixing efficiency measured for different aspect ratios

trapezoidal channels for the following reason. Since the mixing in the microchannels begins from the interface at the channel midline, the trapezoidal edges may not cause a discernable effect on the measurements until the mixing efficiency exceeds a large value for channels with large aspect ratios. All of the mixing efficiency data presented here are lower than 50% except for two of the data points, which are $\eta_{mix} = 57.8$ and 80.5%, measured for $\gamma = 5$ for the lowest flow rate of 0.20 ml/h at $z = 5$ and 15 mm, respectively. It can be seen in Fig. 10b that all measured data fall to compare favorably with the simulations in which the coordinates are shifted to accommodate the difference in aspect ratio as described in Fig. 7. In the non-uniform mixing regime, the experimental results of larger aspect ratios are also better fitted with the curve computed at the surface. Notably, measurements of concentration distribution of the reacted phenolphthalein or fluorescence using conventional microscopy are unable to provide the vertical resolution through the $y$ direction as that of confocal microscopy. The image captured by conventional microscopy, as pointed out by Kamholz and Yager (2001), is a plain picture that integrates the light transmitted and emitted along the vertical direction and may depend, in part, on the depth of focus of the objective lens. During the present measurements of concentration, the focus of the objective lens was adjusted to cover the fluid near the bottom wall for production of clear image. Accordingly, the image captured in the present experiments represents the color intensity for the two-stream mixing occurring in the vicinity of the channel surface rather than the average of the integration over the channel depth. Nevertheless, further careful experiments need to be carried out to examine the quantification of mixing process with conventional microscopy.

## 5 Conclusion

The mixing processes of two fluids in a pressure-driven flow in rectangular microchannels with a wide range of aspect ratio have been analyzed numerically and compared with the measurements of mixing intensity. In the analysis, the 3D species transport equation was using the spectral method with the Chebyshev polynomials in a dimensionless form in which the diffusion coefficient and the average flow velocity together with the axial length and the channel dimension were combined to institute the normalized downstream distance, making the aspect ratio of the channel the only parameter. Solving this dimensionless equation with the highly accurate spectral scheme allows one to efficiently obtain well-resolved species concentration distributions for various aspect ratios and offers clear insight into physics for the micromixing processes. The numerical results show that the mixing intensity determined from the concentration distribution grows with the normalized downstream distance to a power between 0.33 and 0.54 depending on the vertical position and aspect ratio of the mixing channel. The growth power values of the mixing intensity is shown to be essentially the same as that of the width of interdiffusion zone determined with various cutoff concentration. This indicates that both the mixing intensity and the width of interdiffusion zone can be used to characterize the mixing phenomenon. It is found

that the non-uniformity in mixing across the channel depth, which is identified as the butterfly effect, originates from the top and bottom surfaces and extends toward the center of the channel as the normalized downstream distance increases. The non-uniform mixing phenomenon appears to be more pronounced for the mixing channels with smaller aspect ratios. For the channels with larger aspect ratios, where velocity is mainly described by the parabolic profile as in 2D flow, it is found that the mixing intensity grows with the normalized downstream distance based on two different length scales. In the non-uniform regime, the channel depth is used as the length scale and the mixing intensity can be expressed in a simple relationship for different aspect ratios. When the mixing becomes uniform across the depth, the mixing intensity is scaled on the channel width to follow the same growth as in the case of uniform velocity.

Measurements of mixing efficiency based on the quantity of the phenolphthalein reacted with sodium hydroxide were carried out for the mixing channels fabricated on silicon substrates with lager aspect ratios of 5, 10, and 20. For the square channel (aspect ratio = 1) that was fabricated on a PMMA substrate, the mixing efficiency measurements were based on the fluorescent intensity. Using the conventional microscopes, the experiments are capable of demonstrating the mixing efficiency as a power law of the normalized downstream distance that is inversely proportional to the average flow velocity varied in the measurements. The variations of mixing efficiency measured for different aspect ratios in the large range can be rescaled to fall in with a single curve and are in favorable agreement with the simulations. Moreover, the experimental results in the non-uniform mixing regime appear better portrayed by the simulations calculated at the surface than those at the center or the average intensity. The comparison between the experiments and simulations reveals the capabilities and limitations on the use of conventional microscopes for measuring mixing performance.

**Acknowledgments** The authors would like to thank the financial support for this study from the National Science Council of Taiwan under Contract Number NSC 92-2212-E005-012.

## 6 Appendix 1: Discretization with the Chebyshev polynomials

The concentration $C(\xi, \eta, Z^*)$ is approximated by a truncated double series of Chebyshev polynomials as

$$C(\xi,\eta,Z^*) = \sum_{m=0}^{M}\sum_{n=0}^{N} C_{mn}(Z^*)T_m(\xi)T_n(\eta), \tag{19}$$

where $T_m(\xi)$ and $T_n(\eta)$ denote the Chebyshev polynomials and $C_{mn}$ the expansion coefficient. By choosing the Chebyshev Gauss-Lobato collocation points

$$\xi_i = \cos\frac{i\pi}{M}, \quad \eta_j = \cos\frac{j\pi}{N}, \quad i = 0,1,\ldots,M,\ j = 0,1,\ldots,N, \tag{20}$$

we can form the following discrete transform/inverse transform

$$C_{mn}(Z^*) = \frac{4}{d_i d_m e_j e_n MN}\sum_{i=0}^{M}\sum_{j=0}^{N} C(\xi_i,\eta_j,Z^*)T_m(\xi_i)T_n(\eta_j), \tag{21a}$$

$$C(\xi_i,\eta_j,Z^*) = \sum_{m=0}^{M}\sum_{n=0}^{N} C_{mn}(Z^*)T_m(\xi_i)T_n(\eta_j), \tag{21b}$$

where $d_l = \begin{cases} 2, & l = 0,M, \\ 1, & l = \text{otherwise}, \end{cases}$ and $e_l = \begin{cases} 2, & l = 0,N, \\ 1, & l = \text{otherwise}. \end{cases}$ This means that the truncated double series in Eqs. 21a, 21b will interpolate $C(\xi, \eta, Z^*)$ at the collocation points $(\xi_i,\eta_j)$, $i = 0,1,\ldots,M, j = 0,1,\ldots,N$. Substituting Eqs. 21a, 21b into Eq. 19, $C(\xi, \eta, Z^*)$ can be further expressed as

$$C(\xi,\eta,Z^*) = \sum_{i=0}^{M}\sum_{j=0}^{N} C(\xi_i,\eta_j,Z^*)\phi_i(\xi)\varphi_j(\eta), \tag{22a}$$

where $\phi_i(\xi)$and$\varphi_j(\eta)$ are the Lagrange interpolating polynomials defined as

$$\phi_i(\xi) = \prod_{\substack{l=0,\\ l\neq i}}^{M}\frac{\xi-\xi_l}{\xi_i-\xi_l}, \tag{22b}$$

$$\varphi_j(\eta) = \prod_{\substack{lll=0,\\ l\neq j}}^{N}\frac{\eta-\eta_l}{\eta_j-\eta_l}. \tag{22c}$$

The derivatives

$$\frac{\partial C}{\partial\xi}(\xi_i,\eta_j,Z^*), \frac{\partial^2 C}{\partial\xi^2}(\xi_i,\eta_j,Z^*), \frac{\partial C}{\partial\eta}(\xi_i,\eta_j,Z^*),$$

and

$$\frac{\partial^2 C}{\partial\eta^2}(\xi_i,\eta_j,Z^*)$$

can be obtained as

$$\frac{\partial C}{\partial\xi}(\xi_i,\eta_j,Z^*) = \sum_{m=0}^{M}\sum_{n=0}^{N} C(\xi_m,\eta_n,Z^*)\frac{\mathrm{d}\phi_m}{\mathrm{d}\xi}(\xi_i)\varphi_n(\eta_j), \tag{23a}$$

$$\frac{\partial^2 C}{\partial\xi^2}(\xi_i,\eta_j,Z^*) = \sum_{m=0}^{M}\sum_{n=0}^{N} C(\xi_m,\eta_n,Z^*)\frac{\mathrm{d}^2\phi_m}{\mathrm{d}\xi^2}(\xi_i)\varphi_n(\eta_j), \tag{23b}$$

$$\frac{\partial C}{\partial\eta}(\xi_i,\eta_j,Z^*) = \sum_{m=0}^{M}\sum_{n=0}^{N} C(\xi_m,\eta_n,Z^*)\phi_m(\xi_i)\frac{\mathrm{d}\varphi_n}{\mathrm{d}\eta}(\eta_j), \tag{23c}$$

$$\frac{\partial^2 C}{\partial \eta^2}(\xi_i,\eta_j,Z^*) = \sum_{m=0}^{M}\sum_{n=0}^{N} C(\xi_m,\eta_n,Z^*)\phi_m(\xi_i)\frac{\mathrm{d}^2\varphi_n}{\mathrm{d}\eta^2}(\eta_j), \tag{23d}$$

where $[d\phi_m(\xi_i)/d\xi]$ and $[d\varphi_n(\eta_j)/d\eta]$ are usually denoted as the Chebyshev collocation derivative matrices formulated as

$$(\mathbf{D}_\xi)_{im} = \frac{\mathrm{d}\phi_m}{\mathrm{d}\xi}(\xi_i) = \begin{cases} \frac{\mathrm{d}_i(-1)^{i+m}}{\mathrm{d}_m(\xi_i-\xi_m)}, & i\neq m, \\ \frac{-\xi_m}{2(1-\xi_m^2)}, & 1\le i=m\le M-1, \\ \frac{2M^2+1}{6}, & i=m=0, \\ -\frac{2M^2+1}{6}, & i=m=M, \end{cases} \tag{24a}$$

and likewise

$$\left(\mathbf{D}_\eta\right)_{jn} = \frac{\mathrm{d}\varphi_n}{\mathrm{d}\eta}(\eta_j) = \begin{cases} \frac{e_j(-1)^{j+n}}{e_n(\eta_j-\eta_n)}, & j\neq n, \\ \frac{-\eta_n}{2(1-\eta_n^2)}, & 1\le j=n\le N-1, \\ \frac{2N^2+1}{6}, & j=n=0, \\ -\frac{2N^2+1}{6}, & j=n=N. \end{cases} \tag{24b}$$

The second derivative collocation matrices can then be obtained as

$$\frac{\mathrm{d}^2\phi_m}{\mathrm{d}\xi^2}(\xi_i) = \left(\mathbf{D}_\xi^2\right)_{im}, \tag{25a}$$

$$\frac{\mathrm{d}^2\varphi_n}{\mathrm{d}\eta^2}(\eta_j) = \left(\mathbf{D}_\eta^2\right)_{jn}. \tag{25b}$$

The boundary and initial conditions associated with the discretized equation are written as

$$C(-1,\eta_j,Z^*) = 1, \quad \frac{\partial C}{\partial \eta}(\xi_i,\pm 1,Z^*) = \frac{\partial C}{\partial \xi}(1,\eta_j,Z^*) = 0, \quad i=0,1,\ldots,M,\ j=0,1,\ldots,N, \tag{26a}$$

$$C(\xi_i,\eta_j,0) = 0, \quad i=0,1,\ldots,M,\ j=0,1,\ldots,N, \tag{26b}$$

The actual computations of these derivatives can be done alternatively by the transform and inverse transform in Eqs. 21a, 21b, which can speed up via FFT. The details are referred to Canuto et al. (1988) and Trefethen (2000).

## 7 Appendix 2: Rescaling the coordinates for parabolic velocity profile

For the channel with large $\gamma$, where the velocity is portrayed as a parabolic profile, Eq. 7a is rewritten as

$$\frac{3}{2}(1-4Y^2)\frac{\partial C}{\partial Z^+} = \frac{\partial^2 C}{\partial \chi^2} + \frac{\partial^2 C}{\partial Y^2}, \tag{27}$$

where the downstream distance is rescaled as $Z^+ = \gamma^2 Z^* = Dz/(h^2 u_0)$, in reference to the channel depth instead of the channel width, and the dimensionless width is in the small scale $\chi = \gamma X$. Notably, Eq. 27 now does not contain $\gamma$, i.e. independent of aspect ratio. Equation 27 is then solved with the same boundary conditions of Eq. 7b for the concentration $C(\chi, Y, Z^+)$ and the mixing intensity can be obtained by integrating $C(\chi, Y, Z^+)$ over $\chi$ from the midline ($\chi = 0$) to the outer limit ($\chi = \pm\delta/2h$) of the concentration boundary layer,

$$I_{\mathrm{mix}}(Y,Z^+) = \frac{1}{\gamma}\left[\int_{\frac{-\delta}{2h}}^{0} C'(\chi,Y,Z^+)\mathrm{d}\chi + \int_{0}^{\frac{\delta}{2h}} C(\chi,Y,Z^+)\mathrm{d}\chi\right], \tag{28a}$$

or

$$\gamma I_{\mathrm{mix}}(Y,Z^+) = \int_{\frac{-\delta}{2h}}^{0} C'(\chi,Y,Z^+)d\chi + \int_{0}^{\frac{\delta}{2h}} C(\chi,Y,Z^+)\mathrm{d}\chi, \tag{28b}$$

where $\delta$ is taken as the dimensional width of interdiffusion region with a very small cutoff concentration (e.g. 1% or less). Then the product of $I_{\mathrm{mix}}$ and $\gamma$ given by Eq. 28b is independent of aspect ratio until $\delta$ becomes large enough to touch the sidewalls.

## References


Bird R, Stewart W, Lightfoot E (1960) Transport phenomena. Wiley, New York

Bottausci F, Mezic I, Meinhart CD, Cardonne C (2004) Mixing in the shear superposition micromixer: three-dimensional analysis. Philos Trans R Soc Lond A Math Phys Eng Sci 362:1001–1018

Branebjerg J, Gravesen P, Krog JP, Nielsen CR (1996) Fast mixing by lamination. In: Proceedings of the IEEE Micro Electro Mechanical Systems (MEMS), San Diego, USA, pp 441–446

Canuto C, Hussaini MY, Quarteroni A, Zang TA (1988) Spectral methods in fluid dynamics. Springer, Berlin Heidelberg New York

Chen Z, Gao Y, Su R, Li C, Lin J-M (2003) Fabrication and characterization of poly(methyl methacrylate) microchannel by in-situ polymerization method with novel metal template. Electrophoresis 24:3246–3252

Deval J, Tabeling P, Ho C-M (2002) A dielectrophoretic chaotic mixer. In: Proceedings of the IEEE Micro Electro Mechanical Systems (MEMS), Las Vegas, USA, pp 36–39

Gobby D, Angeli P, Gavriidis A (2001) Mixing characteristics of T-type microfluidic mixers. J Micromech Microeng 11:126–132

Gottlieb D, Orszag SA (1997) Numerical analysis of spectral methods: theory and applications. SIAM, Philadelphia

Horng R-H, Han P, Chen H-Y, Lin K-W, Tsai T-M, Zen J-M (2005) PMMA-based capillary electrophoresis electrochemical detection microchip fabrication. J Micromech Microeng 15:6–10

Ismagilov RF, Stroock AD, Kenis PJA and Whitesides GM, Stone HA (2000) Experimental and theoretical scaling laws for transverse diffusive broadening in two-phase laminar flows in microchannels. Appl Phys Lett 76:2376–2378

Kamholz AE, Yager P (2001) Theoretical analysis of molecular diffusion in pressure-driven laminar flow in microfluidic channels. Biophys J 80:155–160

Lee Y-K, Deval J, Tabeling P, Ho C-M (2001) Chaotic mixing in electrokinetically and pressure driven micro flows. In: Proceedings of the IEEE micro electro mechanical systems (MEMS), Interlaken, Switzerland, pp 483–486

Lide DR (1994) CRC handbook of chemistry and physics. CRC Press, Boca Raton

Liu RH, Stremler MA, Sharp KV, Olsen MG, Santiago JG, Adrian RJ, Aref H, Beebe DJ (2000) Passive mixing in a three-dimensional serpentine microchannel. J Microelectromech Syst 9:190–197

Lu R, Ryu K, Liu C (2002) A magnetic microstirrer and array for microfluidic mixing. J Microelectromech Syst 11:462–469

Nguyen N-T, Wu Z (2005) Micromixers—a review. J Micromech Microeng 15:R1–R16

Okkels F, Tabeling P (2004) Spatiotemporal resonances in mixing of open fluids. Phys Rev Lett 92(3):038301-1-4

Qu W, Mala GM, Li D (2000) Pressure-driven water flows in trapezoidal silicon microchannels. Int J Heat Mass Transf 43:353–364

Senturia SD (2001) Microsystem design. Kluwer, Boston

Stone HA, Stroock AD, Ajdari A (2004) Engineering flows in small devices: microfluidics toward a lab-on-a-chip. Annu Rev Fluid Mech 36:381–411

Stroock AD, Dertinger SKW, Ajdari A, Mezic I, Stone HA, Whitesides GM (2002) Chaotic mixer for microchannels. Science 295:647–651

Trefethen L (2000) Spectral methods in Matlab. SIAM, Philadelphia

White FM (1974) Viscous fluid flow. McGraw-Hill, New York

Wu Z, Nguyen N-T, Huang X (2004) Nonlinear diffusive mixing in microchannels: theory and experiments. J Micromech Microeng 14:604–611